ML-Driven Discovery of Metastable States

Yu Zhang
Department of Physics
University of Florida
2001 Museum Rd, Gainesville FL 32611
yuzhang1@ufl.edu

Guanzhi Li
Stanford Institute for Materials and Energy Sciences
SLAC National Laboratory
2575 Sand Hill Rd, Menlo Park, CA 94025
guanzhil@stanford.edu

Minkyung Han
Stanford Institute for Materials and Energy Sciences
SLAC National Laboratory
2575 Sand Hill Rd, Menlo Park, CA 94025
mhan8@stanford.edu

Sean Gasiorowski
SLAC National Laboratory
2575 Sand Hill Rd, Menlo Park, CA 94025
sgaz@slac.stanford.edu

Daniel Ratner
SLAC National Laboratory
2575 Sand Hill Rd, Menlo Park, CA 94025
dratner@slac.stanford.edu

Chunjing Jia
Department of Physics
University of Florida
2001 Museum Rd, Gainesville FL 32611
cjia1@ufl.edu

Yu Lin
Stanford Institute for Materials and Energy Sciences
SLAC National Laboratory
2575 Sand Hill Rd, Menlo Park, CA 94025
lyforest@stanford.edu

Abstract

Metastable states and their minimum energy pathways (MEPs) are central to understanding transformations and phase stability in complex materials, yet exploring them in a wide pressure-temperature space remains computationally demanding and experimentally challenging. While machine learning (ML) offers acceleration beyond conventional density functional theory (DFT), progress requires benchmarks that capture real-world complexity and enable robust method comparisons. Here, we advance the solid-state nudged elastic band (SSNEB) approach by integrating modern ML with DFT for energy, force, and stress evaluations, achieving a 2-3-fold speedup while converging to the same pathways predicted by first-principles calcu-

39th Conference on Neural Information Processing Systems (NeurIPS 2025) Workshop: .

lations. This framework allows systematic benchmarking, providing both efficiency and reliability in predicting MEPs for diverse solid-state material systems.

1 Introduction

Understanding the minimum energy pathways (MEPs) between states and structures is a fundamental problem across materials science, physics, and chemistry. These pathways provide insights into transition mechanisms, energy barriers, kinetic properties, and metastable intermediate states that can be stabilized under external conditions, such as high pressure. Metastable phases often exhibit properties superior to those of their thermodynamically stable counterparts, providing opportunities to design new materials and discover novel states and functionalities for applications ranging from photovoltaics and superconductors to superhard and lightweight engineering materials. Efficiently exploring this vast landscape of stable and metastable states, especially across a wide pressure–temperature (P-T) phase space, is a central challenge in materials discovery.

The nudged elastic band (NEB) method has become a popular tool for probing MEPs by connecting the initial and final states through a chain of images and optimizing the pathway under artificial spring constraints. Conventional NEB is formulated primarily for molecular or finite systems, making it less suitable for periodic solids where lattice degrees of freedom and stress tensors must be considered. To address this, Sheppard et al. [1] generalized the definition of geometric distances and forces in NEB to explicitly include lattice vectors and stress tensors (forces on the lattice vectors), and introduced the solid-state nudged elastic band (SSNEB) method.

Despite its advantages for periodic systems, SSNEB is significantly more computationally demanding than standard NEB, as each image requires accurate energy and force evaluations that include both atomic and lattice degrees of freedom. While ML surrogates have been widely introduced to accelerate conventional NEB, for example, Gaussian Process models and neural network potentials that reduce the number of expensive DFT evaluations along the pathway [2, 3], explicit integration of ML models into SSNEB is, to our knowledge, entirely new.

Here, we present an integrated ML-DFT framework tailored for SSNEB calculations shown in Fig. 1a. By testing several material systems and transition pathways, we demonstrated the validity of our framework and gained insight into the strengths and limitations of the existing ML models.

The algorithmic flow of the SSNEB is illustrated in Fig. 1b. In each iteration, a set of intermediate images (structural configurations connecting the initial and final states) was generated. For each image, energy, atomic forces, and stresses were evaluated using the chosen calculator. Based on the adopted calculators, we have DFT-based and ML-based SSNEB. A combination of forces on the atoms, including spring forces and forces related to the stress and lattice degrees of freedom, was considered. The total force on an atom is given by: $F^{\mathrm{NEB}} = F^{\mathrm{spring}\parallel} + F^{(\text{scaled stress+atomic forces})\perp}$. SSNEB calculations were converged when the total force on any atom in any image was less than $0.01\,\mathrm{eV/\AA}$.

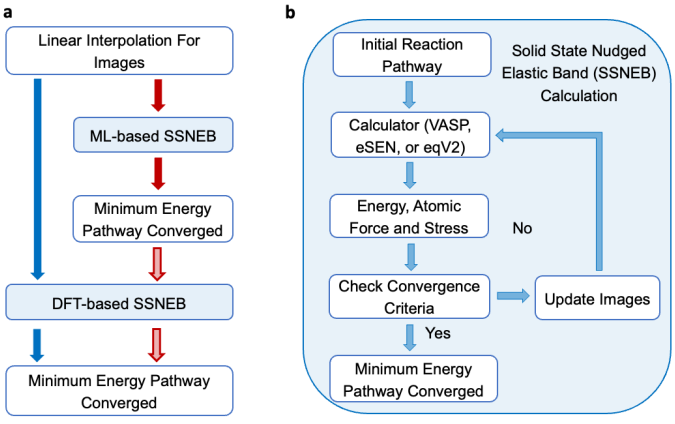

Figure 1: Flowchart of our ML-based SSNEB approach. **a**, blue arrows indicate the traditional approach, where images are generated by linear interpolation, followed by DFT calculations. Red arrows represent our ML-based SSNEB, where MEP is first obtained using model-only calculations (solid arrow), and then refined by restarting DFT-based SSNEB from converged images (hollow arrow). **b**, Algorithm of the SSNEB method.

2 Methods

In this work, we implement ML models of two specific architectures, EquiformerV2 (eqV2) [4] and equivariant Smooth Energy Network (eSEN) [5], as DFT surrogates, serving as the calculators in place of DFT calculations. The eqV2 model used was the 153 million-parameter version (eqV2-L-OMat), which was pretrained on the OMAT dataset [4]. The eSEN model, which has 30 million parameters, was used with the eSEN-30M-OMat variant. This model was also pretrained on the OMAT dataset. All model predictions were performed using a random seed of 42.

Our new ML-based SSNEB framework modifies the conventional SSNEB workflow by integrating ML models into the pathway search (Fig. 1). In the traditional method, images connecting the initial and final states are generated by linear interpolation and evaluated directly with DFT, which is computationally expensive. In contrast, our approach first employs ML models to compute the MEP based exclusively on model evaluations. Once this approximate pathway is obtained, the calculation is refined by restarting SSNEB with DFT, beginning from the ML-converged images. This hybrid workflow reduces the overall computational cost while preserving the accuracy of DFT-based pathways.

3 Results

We validated the framework on two selected test systems, a halide perovskite $CsPbI_3$ and TiO_2. These systems were chosen for their scientific interest, the diversity of their stable and metastable phases, the availability of prior knowledge, and the feasibility of experimental validation, therefore enabling an iterative and reliable evaluation process.

3.1 $CsPbI_3$ results

Halide perovskites represent an extensive family of materials that have received extraordinary research attention due to their remarkable structural, optical, and electronic properties applicable to a wide range of technologies needed for a sustainable energy future. Structurally, 3D halide perovskites have the general formula ABX_3 (X = Cl, Br, I) and adopt an $CaTiO_3$ structur, where the anionic network of corner-sharing B-X octahedra is charge balanced by small organic or inorganic A-site cations [6]. Their soft lattice, characterized by low bulk moduli due to the halogen anions, results in dramatic structure and property changes under external stimuli such as pressure [7].

$CsPbI_3$, an all-inorganic halide perovskite, is particularly attractive because its 3D perovskite phases exhibit optimal bandgaps suitable for photovoltaic applications along with chemical stability against heat and humidity. However, the small size of the Cs^+ ion induces phase instability, where the three perovskite "black" phases with corner-sharing octahedra - cubic α-phase, tetragonal β-phase, and orthorhombic γ-phase - spontaneously transform to the non-perovskite "yellow" δ-phase with edge-sharing octahedra at room temperatures, losing the functionality (Fig. 2a) [8].

Prior experimental work presented a high-pressure strategy to engineer octahedral tilting and manipulate the phase (meta)stability of $CsPbI_3$ for the synthesis and recovery of the metastable perovskite δ-phase with enhanced functionality to ambient conditions [9]. Complementary ML work further validated the predictive power of various models, especially GNNs, for capturing key physical properties such as bandgap and enthalpy of $CsPbI_3$ at high pressure, establishing it as a benchmark system for ML-driven materials discovery [10].

In this work, we accelerate the search for optimal phase transition pathways by combining pre-trained ML models on large material databases with the SSNEB method. $CsPbI_3$ is particularly well suited for this study because of its complex energy landscape with multiple competing phases at local minima, which complicates transition path predictions. Figure 2c presents our ML-SSNEB benchmarks for the ambient-pressure β–γ phase transition of $CsPbI_3$. The VASP-converged path serves as the high-resolution reference or ground truth. The ML-model-converged pathways differ from VASP results in terms of the MEP and structural attributes (*i.e.*, octahedral tilting angles, bond lengths). Then, we restart DFT-based SSNEB from ML-model-converged paths, both (eqV2 and eSEN) converged to VASP results with fewer SSNEB iterations. In terms of computational cost, eSEN and eqV2 are dramatically more efficient than VASP; using them for initial convergence followed by a VASP restart significantly reduces the total cost without sacrificing accuracy. However, deviations in stress or force

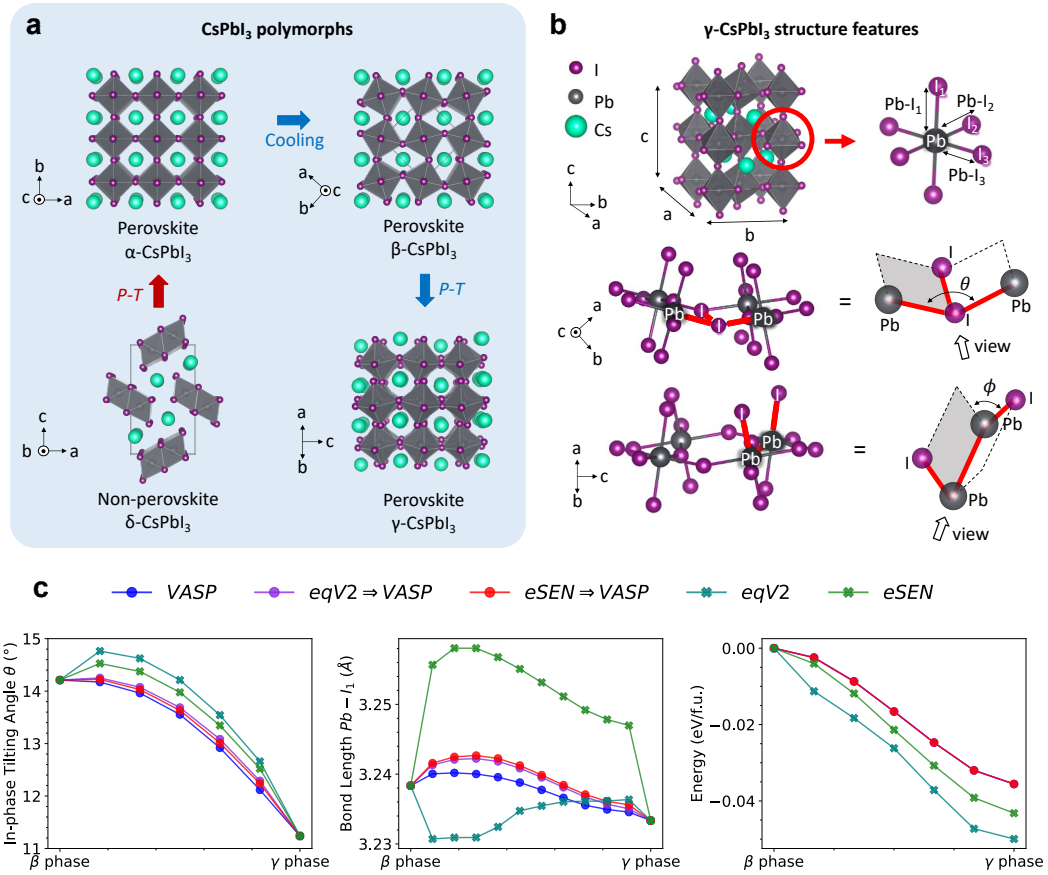

Figure 2: Crystal structures and SSNEB calculations for $CsPbI_3$. **a**, Crystal structures of the α, β, γ, and δ phases, and their phase transitions under varying pressure (P) and temperature (T). **b**, Key structural features of the γ phase, including Pb–I bond lengths, the in-phase octahedral tilting angle (θ), and the out-of-phase tilting angle (ϕ). **c**, SSNEB calculations using five approaches: VASP-based, eqV2 with subsequent VASP restart, eSEN with subsequent VASP restart, eqV2-based, and eSEN-based. Results are shown for the in-phase tilting angle θ, Pb–I_1 bond length, and MEPs.

predictions can accumulate and reduce the structural symmetry, which increases the computational time during the VASP restart. Further details are provided in Table 3 in the Appendix.

3.2 TiO_2 results

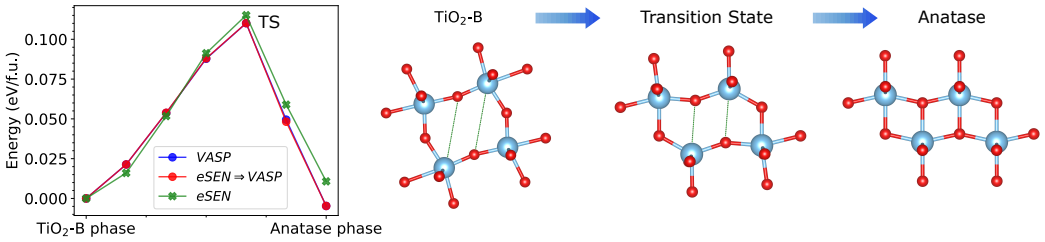

Figure 3: Calculated MEPs from TiO_2-B to anatase phase using three approaches: DFT-based SSNEB, eSEN with subsequent VASP restart, and eSEN-based SSNEB. Right panel shows the crystal structures of the TiO_2-B phase, the transition state at the energy barrier, and the anatase phase.

As another example, we calculate the MEP for TiO_2, a material known to exhibit multiple phases, including TiO_2-B and anatase. Figure 3 presents the MEPs obtained using three approaches: DFT-based SSNEB, the eSEN method with subsequent VASP restart, and eSEN-based SSNEB. All three methods capture the key features of the TiO_2-B to anatase transformation, with the transition state at the saddle point of the energy barrier clearly resolved. The VASP-only approach provides a high-resolution energy barrier of 0.88 eV using the climbing-image SSNEB method, but it is also the most computationally demanding. The eSEN-only pathway yields a slightly higher barrier of 0.92 eV, yet still reproduces the qualitative feature of the transition at dramatically reduced cost. In contrast, the eSEN + VASP restart approach delivers an energy barrier identical to the VASP-only result (0.88 eV) while reducing the computational cost by a factor of 0.72. See Table 5 in the Appendix for more details. These comparisons demonstrate that incorporating eSEN into the workflow offers an efficient strategy for exploring complex phase transitions without compromising accuracy.

4 Discussion and outlook

Our results establish that pre-trained models using eqV2 and eSEN architectures enable reliable convergence in SSNEB calculations for identifying both transition pathways and energy barriers. Between the two, eSEN demonstrates consistently superior performance, offering greater stability and accuracy in mapping the pathway. Importantly, when restarted with VASP, the SSNEB calculations achieve results comparable to high-resolution VASP-only simulations, but with a 2–3-fold gain in computational efficiency. This efficiency is especially striking given that the models were applied without any fine-tuning or transfer learning tailored to the specific materials under investigation. These findings highlight the promise of ML-based SSNEB frameworks as scalable tools for accelerating transition-state searches in complex materials.

Looking ahead, fine-tuning with DFT in active-learning loops or with *ab initio* molecular dynamics offers a natural path to further improve efficiency, particularly for material-specific systems. A central challenge will be optimizing the relative weights in the model to balance accuracy in energies, forces, and stresses, thereby improving the quality of SSNEB total forces. With the rapid advances in ML, we also anticipate that newer pre-trained models will surpass current ones and, when integrated, further enhance the ML-SSNEB framework. By advancing along these directions, this framework has the potential to transform how transition pathways and metastable states are resolved across functional materials for a diverse chemistries and polymorphic phases stabilized under extreme conditions, guiding efficient synthesis and materials discovery.

References

[1] Daniel Sheppard, Penghao Xiao, William Chemelewski, Duane D. Johnson, and Graeme Henkelman. A generalized solid-state nudged elastic band method. *The Journal of Chemical Physics*, 136(7):074103, 02 2012. ISSN 0021-9606. doi: 10.1063/1.3684549. URL `https://doi.org/10.1063/1.3684549`.

[2] José A. Garrido Torres, Paul C. Jennings, Martin H. Hansen, Jacob R. Boes, and Thomas Bligaard. Low-scaling algorithm for nudged elastic band calculations using a surrogate machine learning model. *Phys. Rev. Lett.*, 122:156001, Apr 2019. doi: 10.1103/PhysRevLett.122.156001. URL `https://link.aps.org/doi/10.1103/PhysRevLett.122.156001`.

[3] A Fantasia, F Rovaris, O Abou El Kheir, A Marzegalli, D Lanzoni, L Pessina, P Xiao, C Zhou, L Li, G Henkelman, et al. Development of a machine learning interatomic potential for exploring pressure-dependent kinetics of phase transitions in germanium. *The Journal of Chemical Physics*, 161(1), 2024.

[4] Luis Barroso-Luque, Muhammed Shuaibi, Xiang Fu, Brandon M. Wood, Misko Dzamba, Meng Gao, Ammar Rizvi, C. Lawrence Zitnick, and Zachary W. Ulissi. Open materials 2024 (omat24) inorganic materials dataset and models, 2024. URL `https://arxiv.org/abs/2410.12771`.

[5] Xiang Fu, Brandon M. Wood, Luis Barroso-Luque, Daniel S. Levine, Meng Gao, Misko Dzamba, and C. Lawrence Zitnick. Learning smooth and expressive interatomic potentials for physical property prediction, 2025. URL `https://arxiv.org/abs/2502.12147`.

[6] Akihiro Kojima, Kenjiro Teshima, Yasuo Shirai, and Tsutomu Miyasaka. Organometal halide perovskites as visible-light sensitizers for photovoltaic cells. *Journal of the american chemical society*, 131(17):6050–6051, 2009.

[7] Adam Jaffe, Yu Lin, and Hemamala I Karunadasa. Halide perovskites under pressure: accessing new properties through lattice compression. *ACS Energy Letters*, 2(7):1549–1555, 2017.

[8] Constantinos C Stoumpos, Christos D Malliakas, and Mercouri G Kanatzidis. Semiconducting tin and lead iodide perovskites with organic cations: phase transitions, high mobilities, and near-infrared photoluminescent properties. *Inorganic chemistry*, 52(15):9019–9038, 2013.

[9] Feng Ke, Chenxu Wang, Chunjing Jia, Nathan R Wolf, Jiejuan Yan, Shanyuan Niu, Thomas P Devereaux, Hemamala I Karunadasa, Wendy L Mao, and Yu Lin. Preserving a robust cspbi3 perovskite phase via pressure-directed octahedral tilt. *Nature communications*, 12(1):461, 2021.

[10] Minkyung Han, Cheng Peng, Ruyi Song, Feng Ke, Youssef SG Nashed, Wendy L Mao, Chunjing Jia, and Yu Lin. Machine learning-empowered study of metastable γ-cspbi 3 under pressure and strain. *Journal of Materials Chemistry A*, 12(18):11082–11089, 2024.

[11] G. Kresse and J. Hafner. Ab initio molecular-dynamics simulation of the liquid-metal–amorphous-semiconductor transition in germanium. *Phys. Rev. B*, 49:14251–14269, May 1994. doi: 10.1103/PhysRevB.49.14251. URL `https://link.aps.org/doi/10.1103/PhysRevB.49.14251`.

[12] G. Kresse and D. Joubert. From ultrasoft pseudopotentials to the projector augmented-wave method. *Phys. Rev. B*, 59:1758–1775, Jan 1999. doi: 10.1103/PhysRevB.59.1758. URL `https://link.aps.org/doi/10.1103/PhysRevB.59.1758`.

[13] John P. Perdew, Kieron Burke, and Matthias Ernzerhof. Generalized gradient approximation made simple. *Phys. Rev. Lett.*, 77:3865–3868, Oct 1996. doi: 10.1103/PhysRevLett.77.3865. URL `https://link.aps.org/doi/10.1103/PhysRevLett.77.3865`.

[14] Hendrik J. Monkhorst and James D. Pack. Special points for brillouin-zone integrations. *Phys. Rev. B*, 13:5188–5192, Jun 1976. doi: 10.1103/PhysRevB.13.5188. URL `https://link.aps.org/doi/10.1103/PhysRevB.13.5188`.

A Technical Appendices and Supplementary Material

A.1 Methods for DFT calculations

The DFT calculations were performed using the Vienna Ab-initio Simulation Package (VASP) [11], with the projector augmented wave (PAW) [12] method and the Perdew-Burke-Ernzerhof (PBE) [13] exchange-correlation functional. For calculations of $CsPbI_3$, a plane-wave energy cutoff of $600\,\mathrm{eV}$ was used, and the convergence threshold for total energy was set to $1 \times 10^{-8}\,\mathrm{eV}$. For the α-to-β phase transition, a supercell containing two formula units and a $4 \times 4 \times 6$ Monkhorst-Pack [14] k-point mesh was used. Due to the reduced symmetry of the gamma phase, a larger supercell with four formula units and a $4 \times 4 \times 3$ Monkhorst-Pack k-point mesh was used for the α-to-γ and β-to-γ transitions. For calculations of TiO_2, a plane-wave energy cutoff of 500 eV was used, and the convergence threshold for total energy was $1 \times 10^{-6}\,\mathrm{eV}$. A supercell containing 24 atoms and a $4\times4\times4$ Monkhorst-Pack k-point mesh were used in the calculations.

A.2 SSNEB Results and Computational Time

Table 1: Computational Time per Structure for $CsPbI_3$ β to γ Transition.

	VASP	eSEN
32 CPUs	269.98s	0.53s
Single L4 GPU	148.85s	0.39s
Single B200 GPU	191.49s	0.28s

VASP computational time highly depends on the size and symmetry of the cell, while pre-trained model inference time mostly depends on the computational resources.

Table 2: SSNEB Results for $CsPbI_3$ α to β Transition (normal method).

SSNEB Setup		Convergence Iterations		Relative Computing Time	
Initial Path	Calculator	$N_{img} = 5$	$N_{img} = 10$	$N_{img} = 5$	$N_{img} = 10$
Linear	VASP	56	59	1.00	1.00
eqV2	VASP*	25	28	2.40	0.63
eSEN	VASP	25	28	0.55	0.72
Linear	eqV2	62	74		
Linear	eSEN	63	57		

N_{img}: number of intermediate states.

VASP*: Different VASP setups were used when restart from eqV2 converged pathways.
ISYM = 0 / SYMPREC = 10^{-8} for N_{img} = 5 / 10, respectively.

The computational time of using pre-trained models as the calculator is negligible. To estimate the efficiency of ML-SSNEB method, we sum the irreducible k-points used for all images during the SSNEB iterations and compare the total number with that from pure VASP calculations.

Table 3: SSNEB Results for $CsPbI_3$ β to γ Transition (normal method).

SSNEB Setup		Convergence Iterations		Relative Computing Time	
Initial Path	Calculator	$N_{img} = 5$	$N_{img} = 10$	$N_{img} = 5$	$N_{img} = 10$
Linear	VASP	125	235	1.00	1.00
eqV2	VASP*	86	132	2.06	1.66
eSEN	VASP	73	81	0.59	0.35
Linear	eqV2	124	201		
Linear	eSEN	127	239		

VASP*: SYMPREC = 10^{-6} / ISYM = 0 for N_{img} = 5 / 10, respectively.

Table 4: SSNEB Results for $CsPbI_3$ α to γ Transition (normal method).

SSNEB Setup		Convergence Iterations		Relative Computing Time	
Initial Path	Calculator	$N_{img} = 5$	$N_{img} = 10$	$N_{img} = 5$	$N_{img} = 10$
Linear	VASP	186	370	1.00	1.00
eqV2	VASP*	58	81	0.94	0.55
eSEN	VASP	46	55	0.59	0.39
Linear	eqV2	198	371		
Linear	eSEN	173	355		

VASP*: SYMPREC = 10^{-6} / SYMPREC = 10^{-7} for N_{img} = 5 / 10, respectively.

Table 5: CI-NEB Results for TiO_2-B to Anatase Transition. ($N_{img} = 5$)

SSNEB Setup		Convergence Iterations	Energy Barrier (eV)	Relative Computing Time
Initial Path	Calculator			
Linear	VASP	80	0.88	1.00
eSEN	VASP	58	0.88	0.72
Linear	eSEN	82	0.92	

CI-NEB: the climbing-image NEB method, used to locate the saddle point (transition state) along the reaction pathway.

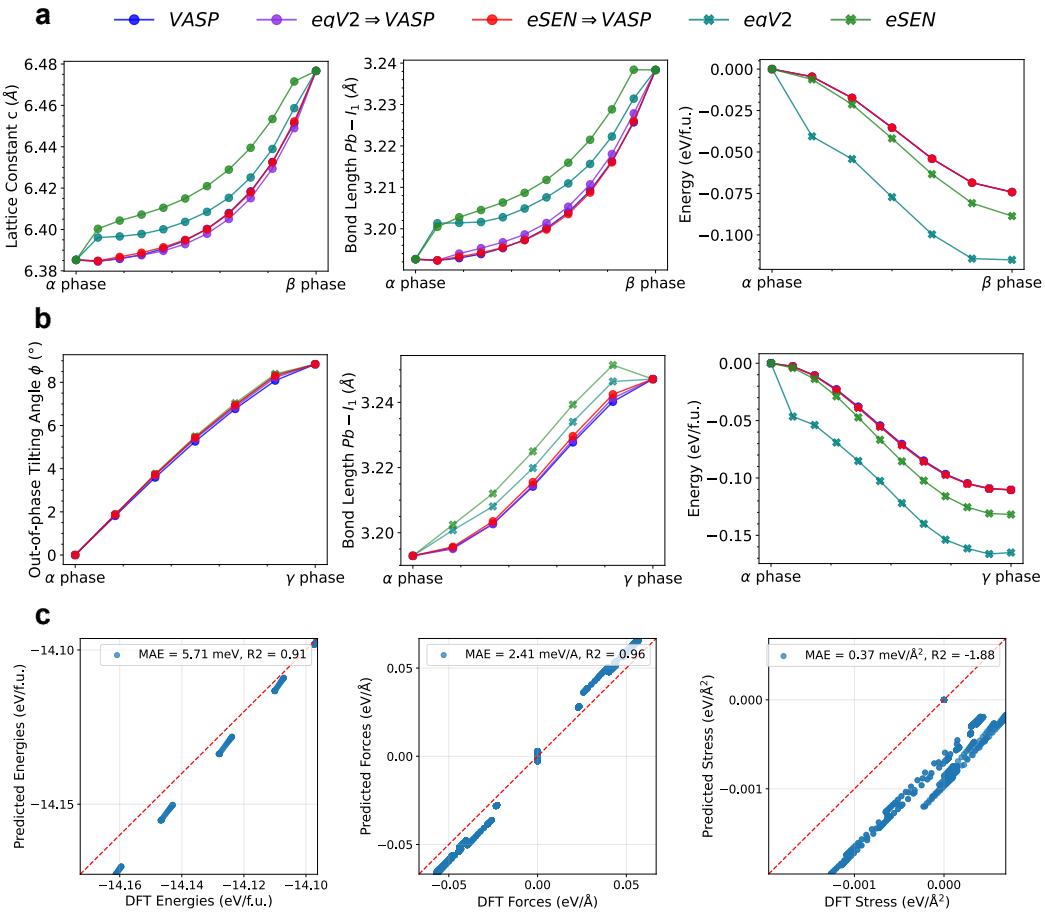

Figure 4: **a** The five $CsPbI_3$ α to β transition pathways obtained from different SSNEB approaches are illustrated. The lattice constant c, Pb–I_1 bond length, and MEPs are presented here. The largest deviations occur in the first and last intermediate structures. **b** Structure features and MEPs for α to γ transition. **c** To directly evaluate the performance of the pre-trained eSEN model, we present parity plots for energy, force, and stress. In these plots, the x-axis represents the EFS values calculated by VASP for the α to β transition (N_{img}=5), while the y-axis shows the corresponding predictions from the eSEN model. Large deviations are observed in the stress predictions, indicating the need for further investigation.